This is a peer-reviewed, accepted author manuscript of the following article: Wang, X., Liu, Z., Cai, Y., Wang, B., & Luo, X. (2021). A cost-effective serpentine micromixer utilizing ellipse curve. *Analytica Chimica Acta*, *1155*, [338355]. https://doi.org/10.1016/j.aca.2021.338355

A cost-effective serpentine micromixer utilizing ellipse curve

Xin Wang [a,b], Zhanqiang Liu [a,b]*, Yukui Cai [a,b], Bing Wang[a,b], Xichun Luo[c]

([a] School of Mechanical Engineering, Shandong University, Jinan 250061, Shandong, China;

[b] Key Laboratory of High Efficiency and Clean Mechanical Manufacture of MOE/Key National Demonstration Center for Experimental Mechanical Engineering Education, Jinan 250061, Shandong, China;

[c] Centre for Precision Manufacturing, DMEM, University of Strathclyde, UK)

*Corresponding author, Telephone: +86-531-88393206, Fax: +86-531-88392045,

Email: melius@sdu.edu.cn

Abstract

Due to high mixing performance and simple geometry structure, serpentine micromixer is one typical passive micromixer that has been widely investigated. Traditional zigzag and square-wave serpentine micromixers can achieve sufficient mixing, but tend to induce significant pressure drop. The excessive pressure drop means more energy consumption, which leads to low cost-performance of mixing. To mitigate excessive pressure drop, a novel serpentine micromixer utilizing ellipse curve is proposed. While fluids flowing through ellipse curve microchannels, the flow directions keep continuous changing. Therefore, the Dean vortices are induced throughout the whole flow path. Numerical simulation and visualization experiments are conducted at Reynolds number

(Re) ranging from 0.1 to 100. Dean vortices varies with the changing curvature in different ellipse curves, and local Dean numbers are calculated for quantitative evaluation. The results suggest that the ellipse with a larger eccentricity induces stronger Dean vortices, thus better mixing performance can be obtained. A parameter, named mixing performance cost (*Mec*), is proposed to evaluate the cost- performance of micromixers. Compared with the zigzag, square-wave and other improved serpentine micromixers, the ellipse curve micromixer produces lower pressure drop while have the capability to maintain excellent mixing performance. The ellipse curve micromixer is proved to be more cost-effective for rapid mixing in complex microfluidic systems.

Key words: Micromixer; Ellipse curve; Dean number; Mixing performance; Pressure drop; Mixing efficiency cost

1. Introduction

Owing to tiny size and strong functional integration, the microfluidic system presents the superiorities of less reagent consumption and higher reaction efficiency. As an essential component of the microfluidic system, micromixers are employed to achieve the efficient mixing of various reagents. With rapid development of nano- and micro-processing technologies, micromixers have been not only widely applied in chemical synthesis [1] and chemical reactions [2], but also in biomedical processes [3], including cell manipulation [4], DNA analysis [5] and protein detection [6]. However, due to the limitation of microscale, flows in micromixers are always steady laminar flows. Mixing mainly depends on molecular diffusion especially at low Reynolds

numbers, which is a slow and inefficient process. To obtain a fast and sufficient mixing, various micromixer strategies have been put forward.

Micromixers are categorized into two types as active and passive ones. Active micromixers take use of external energy sources including acoustic [7], electric [8], pressure [9], thermal [10] and magnetic fields [11] to agitate the flow fields and promote mixing. Passive micromixers utilize specially designed structures to disturb the flow fields and generate chaotic advection. Independent on external energy, passive micromixers are more environmental-friendly. Compared with the active micromixers, passive micromixers have simpler structure and smaller size, thus they are easier to manufacture and flexible to integrate with other functional components. A variety of effective structures about the passive micromixers have been proposed, such as obstacles and baffles [12,13], grooves [14], multi-layers [15], mixing chambers [16,17] and splitting and recombining structures (SAR) [18-20].

Among various passive micromixers, serpentine microchannel is the simplest and most effective structure. In serpentine micromixers, zigzag, square-wave and circular serpentine microchannels are the three basic structures that used most commonly [21]. Based on the three basic serpentine microchannels, various novel structures are proposed to improve the mixing performance. Elmas et al. [22] used simple serpentine microchannels for online swimming pool monitoring with a special design. By mixing water with two chemical reagents (methyl orange and phenol red), both chlorine content and PH of the swimming pool would be indicated.

For zigzag serpentine micromixers, Mengeaud et al. [23] investigated the

influence of geometry parameters on the mixing performance. The most homogeneous mixing could be obtained when the ratio of periodic step to width equaled four. Chen and Li [24] added obstacles to zigzag microchannels so as to generate reversed flows. A topology optimization method was also employed to determine the optimal structure. As a result, the optimized micromixer could achieve better mixing performance than the traditional zigzag micromixer, but the pressure drop of the optimized micromixer was also higher than that of the traditional one. In the same way, similar obstacles and topology optimization method were also applied on the square-wave micromixer [25]. By adding the obstacles, the minimum mixing performance of the improved micromixer was even higher than 80%. However, the improved micromixer produced much higher pressure drop at the same time, which added the burden of the microfluidic system.

Derived from the traditional square-wave structure, Hossain and Kim [26] used the non-aligned inputs to improve the mixing performance. Although better mixing performance was achieved, the use of non-aligned inputs induced higher pressure drop at the same time. Kuo et al. [27] designed a square-wave serpentine micromixer on a rotating compact disk. In their research, the rotating micromixer could realize an effective mixing between blood plasma and Deionized water when given a rotation speed of 2,000 rpm. Moreover, Shamloo et al. [28] investigated the square-wave serpentine microchannels with different cross-sectional profiles. Their results showed that the vertical triangular cross section had the best mixing performance while the horizonal rectangular section had the worst.

Likewise, Clark et al. [29] put forward a circular serpentine micromixer with non-rectangular cross sections. In the step-like non-rectangular cross sections, the original symmetry vortices were broken and extra vortices were formed, thereby achieving a more homogeneous mixing. Cook et al. [30] combined the slanted grooves with circular serpentine microchannels, which not only induced Dean vortices but also promoted the formation of helical flows. Similarly, Rhoades et al. [31] introduced asymmetric staggered herring bone grooves into the circular serpentine micromixer. In the asymmetric grooves, orthogonal flows occurred and then encountered with the Dean vortices, making the flow field more complex. In consequence, the chaotic advection was enhanced and better mixing performance could be achieved. However, in consideration of the complex flow fields, their research lacked the evaluation of energy consumed such as pressure drop.

Moreover, Hossain et al. [21] conducted a comparative research on serpentine micromixers with zigzag, square-wave and circular microchannels through numerical simulation. They concluded that the square-wave micromixer could obtain the best mixing performance but simultaneously produced the highest pressure drop. The circular micromixer and the zigzag micromixer got similar mixing performance, while the circular one produced the lowest pressure drop. Furtherly, Chen et al. [32] investigated the mixing performance and pressure drop among zigzag, square-wave and circular serpentine micromixers by both experiments and numerical simulation. In their research, the difference in mixing performance among the three serpentine micromixers was about 5%, and yet the pressure drop of square-wave micromixer was almost twice

that of circular micromixer.

Aside from the zigzag, square-wave and circular serpentine micromixers, Parsa et al. [33] designed a sinusoidal serpentine micromixer with different phase shift. They reported that expansion vortices were generated when the phase shift was $3\pi/4$ and $\pi/2$, leading to a mixing performance above 90%. Similarly, Javaid et al. [34] developed a serpentine micromixer with sinusoidal side walls. When the ratio of amplitude to wave length was higher than 0.15, the sinusoidal micromixer indicated better mixing performance than the square-wave micromixer, but a higher pressure drop occurred at the same time. Moreover, according to the evaluation of mixing cost in their research, the mixing cost of sinusoidal micromixer was higher than that of the square-wave micromixer when $Re \geq 50$.

As mentioned above, for serpentine micromixers, high mixing performance was always accompanied by the cost of high pressure drop. In order to improve the cost-performance of mixing, we propose a novel cost-effective serpentine micromixer utilizing ellipse curve. The relationship among ellipse shapes, mixing performance, and pressure drop has been revealed. Flow behaviors and mixing process are investigated by both intuitive flow patterns and quantitative calculation. A novel parameter named mixing efficiency cost (*Mec*) is presented for the first time to evaluate the cost-performance.

2. Micromixer design

The ellipse curve micromixer utilizes ellipses as the serpentine microchannels, so

the curvature of microchannels is not a constant. As presented in Fig. 1, eight ellipses with four focal length are considered in the research to determine the optimal structure. The circumference of each ellipse is fixed as 6 mm. Only curves above the X-axis are used in the micromixer design. The X-axis points to the mainstream direction and Y-axis the vertical direction. Ellipses 1 to 4 are with foci on the X-axis, as defined by Eq. (1) and shown in Fig. 1(a). The other four ellipses with foci on the Y-axis are defined by Eq. (2) and shown in Fig. 1(b). In addition, since the circle can be regarded as an ellipse that with the major axis equals the minor axis, the traditional circular serpentine micromixer is also included in the research.

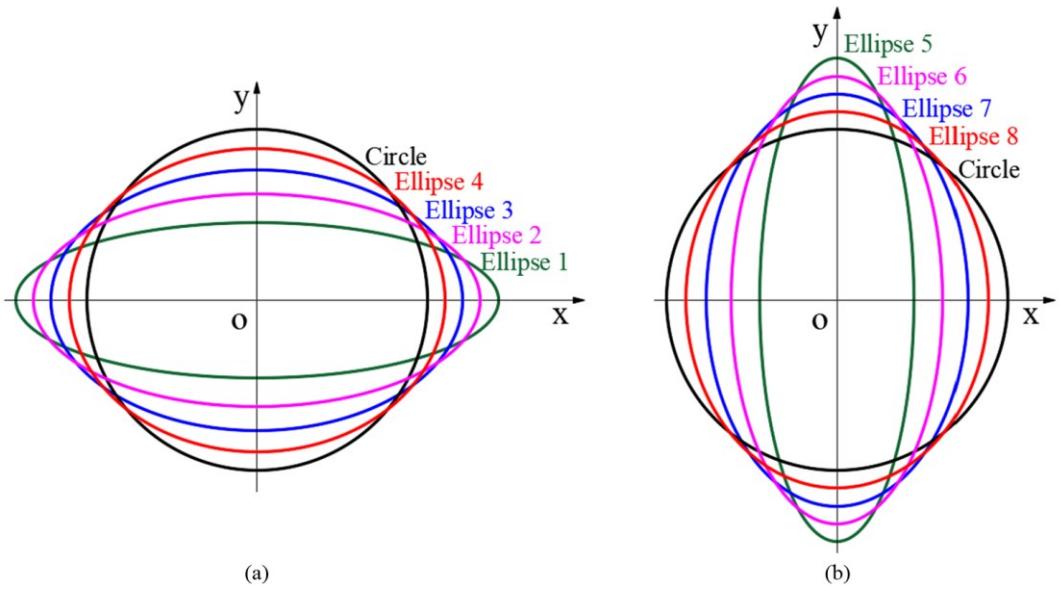

Fig. 1. (a) Ellipses with foci on the X-axis; (b) ellipses with foci on the Y-axis.

$$\frac{x^2}{a^2}+\frac{y^2}{b^2}=1 \quad (a>b>0) \tag{1}$$

$$\frac{y^2}{a^2}+\frac{x^2}{b^2}=1 \quad (a>b>0) \tag{2}$$

where, a is the major axis of ellipse, b the minor axis. Generally, the shape of ellipse

could be described by the eccentricity *e*, defined by Eq. (3).

$$e = \frac{c}{a} = \frac{\sqrt{a^2 - b^2}}{a} \tag{3}$$

where, *c* is half the focal length. As illustrated in Fig. 1, shapes of ellipses 5 to 8 correspond to ellipses 1 to 4. In other words, ellipses 1 and 5 have the same eccentricity, same cases for ellipses 2 and 6, ellipses 3 and 7, and ellipses 4 and 8. A larger eccentricity means that the ellipse is flatter and its curvature varies more. Accordingly, ellipses 1 and 5 have the maximum eccentricity and their curvature have the largest change variation, while in ellipses 4 and 8 the curvature changes the least.

Fig. 2 exhibits the schematic diagrams of the ellipse curve micromixer. Each micromixer has six mixing units. More mixing units result in excessive pressure drop, but little progress in mixing performance because mixing performance will have already been saturated within six mixing units. All the detailed parameters of the ellipse curve micromixer are presented in table 1.

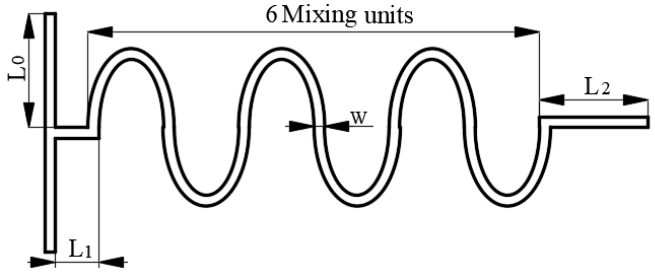

(a) Ellipse curve microchannels with foci on the Y-axis.

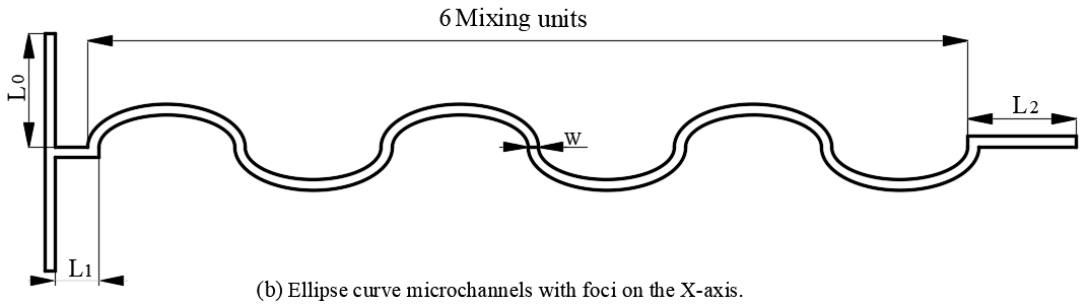

(b) Ellipse curve microchannels with foci on the X-axis.

Fig. 2. Ellipse curve micromixers with foci on the (a) Y-axis and (b) X-axis.

Table 1

Geometry parameters of micromixers utilizing ellipse curve.

Geometry parameters	Value	Dimension
Inlet length (L_0)	2	mm
Straight channel length (L_1)	800	μm
Outlet length (L_2)	1600	μm
Channel width (w)	200	μm
Channel depth (d)	200	μm
Major axis of ellipse 1 and ellipse 5 (a_1, a_5)	1355	μm
Major axis of ellipse 2 and ellipse 6 (a_2, a_6)	1255	μm
Major axis of ellipse 3 and ellipse 7 (a_3, a_7)	1155	μm
Major axis of ellipse 4 and ellipse 8 (a_4, a_8)	1055	μm
Radius of the circle (R)	955	μm
Ellipse circumference (C)	6	mm

For comparative study, the traditional zigzag and square-wave serpentine micromixers have also been analyzed. Both the zigzag and square-wave micromixers are designed with the same parameters to the ellipse curve micromixer, ensuring mixing takes place under the same condition.

3. Fabrication and visualization experiments

The ellipse curve micromixers were fabricated by high-speed micromilling on

PMMA substrates. A micromilling cutter with a diameter of 0.2 mm was adopted in the process, as presented in Fig. 3(a). The spindle speed, feed rate and depth of cut were settled as 20000 rev min^{-1}, 100 mm min^{-1} and 0.05 μm, respectively. After the fabrication, ultrasonic cleaning was employed to remove the burrs and a double-layer force-induced adhesive film was used for the sealing.

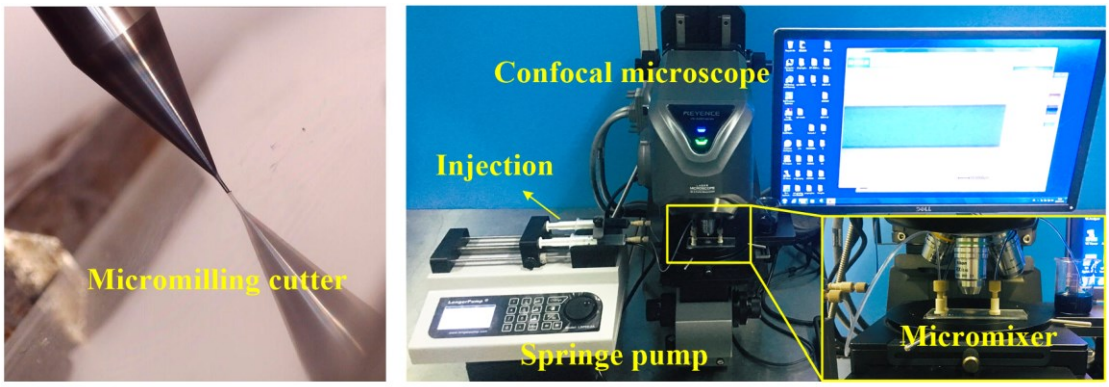

Fig. 3. (a) Micromilling process, (b) visualization experiments.

Fig. 3(b) presents the setup of mixing experiments, where blue aqueous solution and deionized water were chosen as the two miscible reagents. Two steady and continuous flows were supplied into the micromixer via a springe pump. A laser confocal microscope was fixed to take snapshots of mixing at the outlet of micromixers. Then, mixing images were processed by the ImageJ software to evaluate the mixing performance.

4. Numerical simulation

The flow fields and mixing process of ellipse curve micromixers have been investigated by numerical simulation, carried out on COMSOL Mutiphysics 5.3a software. Assuming that the mixing fluids are incompressible Newtonian fluids, the

flow model can be described by the three-dimensional Navier-Stokes equation and continuity equation, expressed in Eqs. (4) and (5).

$$\nabla \cdot \vec{V} = 0 \tag{4}$$

$$\rho\left(\vec{V} \cdot \nabla\right)\vec{V} = -P + \mu\nabla^2\vec{V} \tag{5}$$

where, $\vec{V}$ represents the flow velocity, μ the dynamic viscosity, ρ the fluid density, and P denotes the pressure. The concentration distribution in micromixers is modeled according to the convection-diffusion equation, expressed in Eq. (6).

$$(\vec{V} \cdot \nabla)c = D\nabla^2 c \tag{6}$$

where, D and c are the fluid diffusion coefficient and the concentration, respectively. For the sample fluid used in our research, fluid density ρ, dynamitic viscosity μ and diffusion coefficient D are settled as 9.97×10^2 kg m^{-3}, 0.9×10^{-3} Pa s and 2.97×10^{-10} m^2 s^{-1}, respectively. Reynolds number (Re) that represents the flow conditions is described as Eq. (7).

$$Re = \frac{\rho V D_h}{\mu} \tag{7}$$

where, D_h is the hydraulic diameter of microchannels and V is the average flow velocity. No-slip boundary conditions are applied and the static pressure at the outlet is set to be zero. Two inlets are assigned with fluid concentration of 1 mol L^{-1} and 0, respectively. Mixing performance of micromixers is calculated in accordance to the variance of concentration mass fraction (σ), which is defined by Eq. (8). And the mixing performance (M) is defined by Eq. (9).

$$\sigma = \sqrt{\frac{1}{N}\sum_{i=1}^{N}(c_i - \overline{c_m})^2} \tag{8}$$

$$M = 1 - \sqrt{\frac{\sigma^2}{\sigma_{\max}^2}} \tag{9}$$

where, c_i represents the concentration mass fraction of each sampling point, and $\overline{c_m}$ is the concentration mass fraction when two fluids are fully mixing. Mixing performance (M) ranges from 0 (when $\sigma = \sigma_{max}$, no mixing) to 1 (when $\sigma = 0$, fully mixing).

5. Grid independence test and experimental validation

5.1. Grid independence test

Since the results of numerical simulation are influenced by meshing methods, the grid independence test needs to be carried out to determine the optimal meshing method. In this research, the grid independence test was conducted among five meshing methods, of which grid numbers ranging from 36,671 to 2,168,025. Both the Navier-Stokes equation and the convection-diffusion equation are tested. Fig. 4 and Fig. 5 exhibit the velocity distribution and the concentration distribution of the centerline in outlet cross-sectional plane, respectively.

As shown in Fig. 4, the velocity distribution with a grid number of 1,240,348 is quite similar to the velocity distribution with a grid number of 2,168,025. The maximum error between the two curves is within 1%. Moreover, as shown in Fig. 5, the concentration distributions are very close when the grid numbers are 2,168,025, 1,240,348 and 607,830. Especially when the grid numbers are 2,168,025 and 1,240,348, the maximum error is only 0.7%. Therefore, to maintain the accuracy and efficiency at the same time, the meshing method with a grid number of 1,240,348 is chosen for the

numerical simulation.

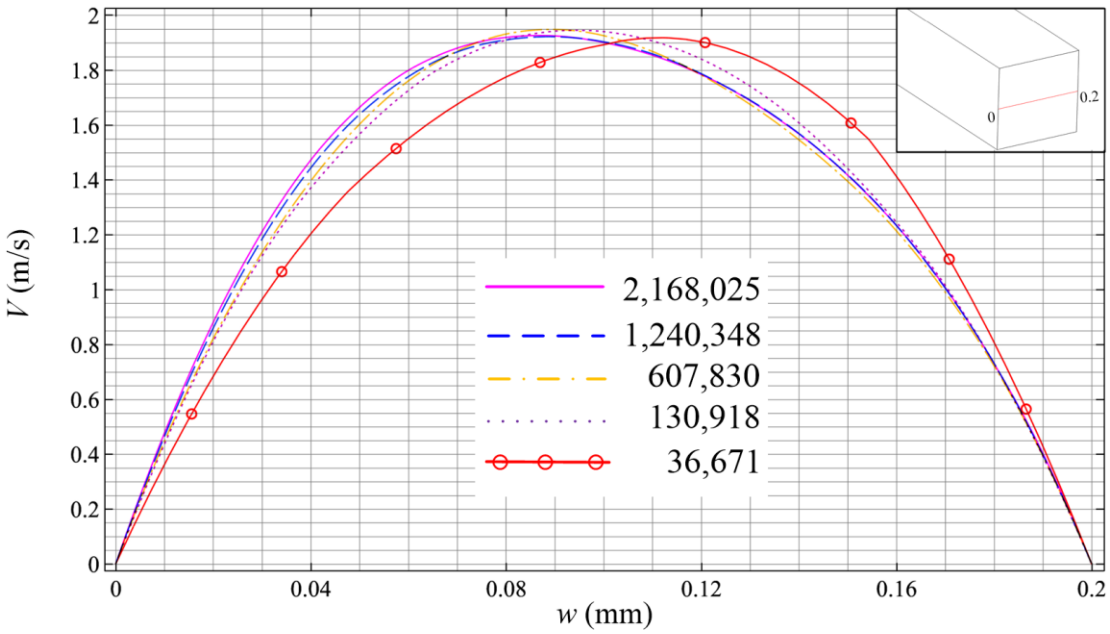

Fig. 4. Velocity distribution of the centerline in outlet cross-sectional plane at Re = 100.

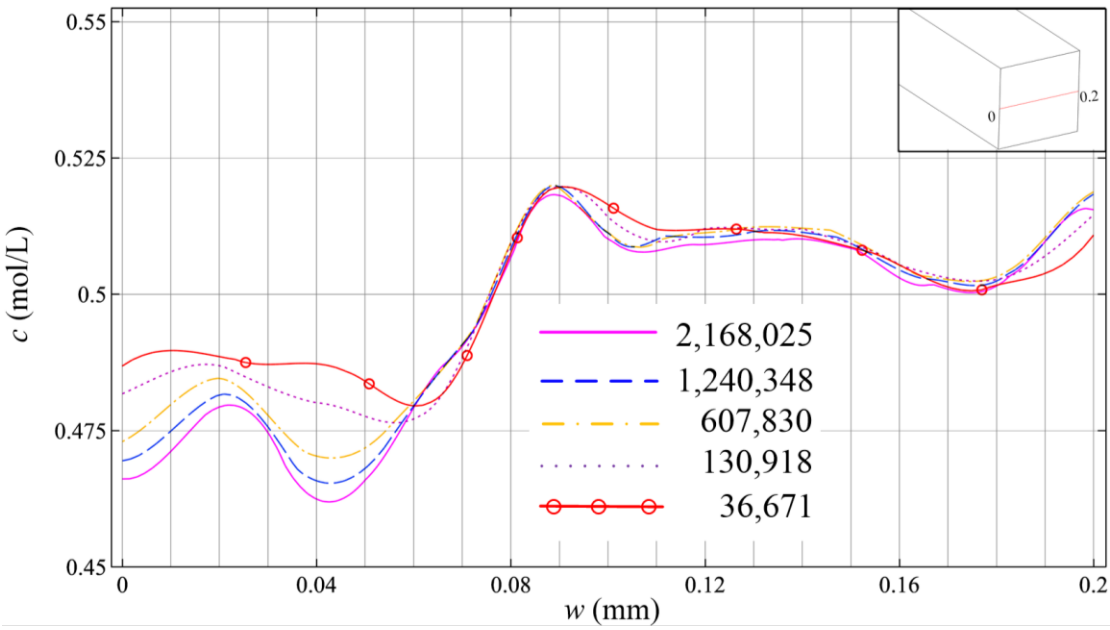

Fig. 5. Concentration distribution of the centerline in outlet cross-sectional plane at Re = 100.

5.2. Experimental validation

The numerical simulation is validated by various visualization experiments with *Re* from 0.1 to 100. Fig. 6 compares the mixing performance from numerical simulation

and experiments. It can be seen that the numerical results agree well with the experimental results. The maximum difference between the experimental and numerical results is about 2%, which only occurs at Re = 30 and Re = 50.

The difference between the experimental and numerical results mainly results from two aspects. On the one hand, there are surface defects generated in the manufacturing process, thus the actual microchannels are not exact smooth as the geometric model used in numerical simulation. On the other hand, the mixing performance of numerical simulation is calculated based on the cross-sections of the outlet, while the mixing performance of experiments is calculated based on the top view mixing images (as shown in Fig. 7). The top view mixing images measured by the confocal microscope are three-dimensional superposition of different focus levels, which could reflect the concentration distribution. Since it is hard to get the mixing images of cross sections, as an alternative method, the experimental mixing performance is calculated based on the top view mixing images.

Additionally, Fig. 7 shows the grayscale mixing images of the micromixer with ellipse 2 from the top view direction. It is observed from Fig. 7(b) that mixing begins from the centerline of the microchannel where the two samples contact with each other. As mixing develops, the boundary of two samples becomes blurred. When the mixing performance reaches 90%, the boundary is completely disappeared in the top view images, as seen from Fig. 7(a) and (d).

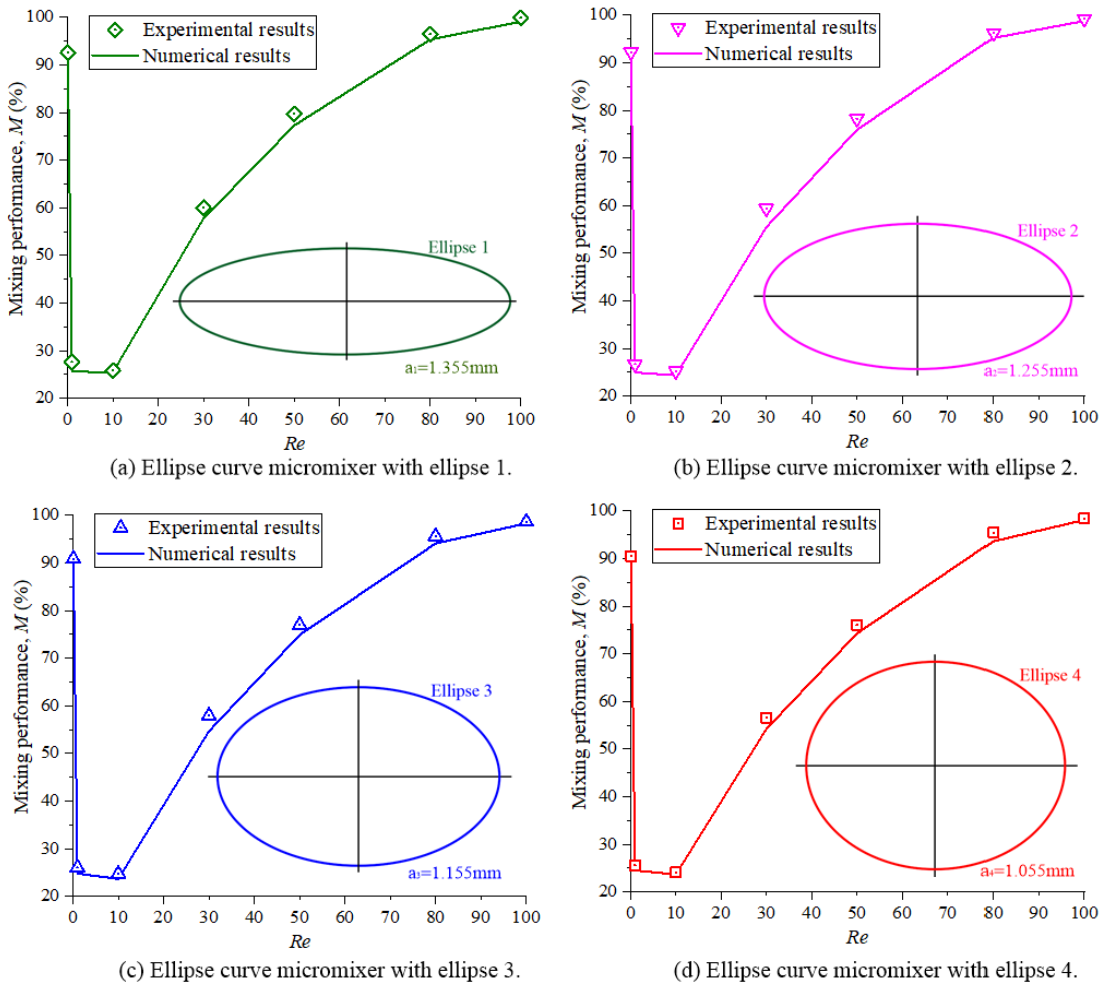

Fig. 6. Experimental and numerical results of mixing performance with *Re* from 0.1 to 100.

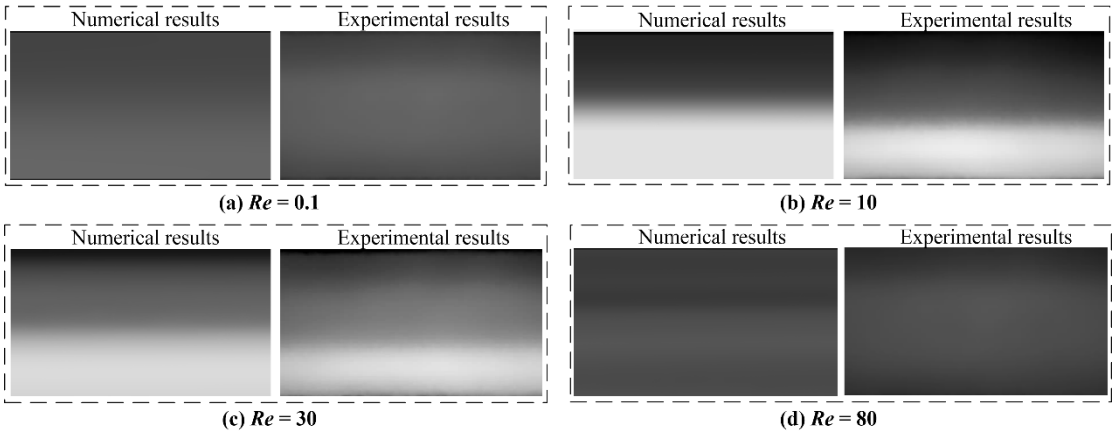

Fig. 7. Top view grayscale images at the outlet of ellipse curve micromixer with ellipse 2.

6. Results and discussion

6.1. Mixing performance

6.1.1. Effects of Reynolds number

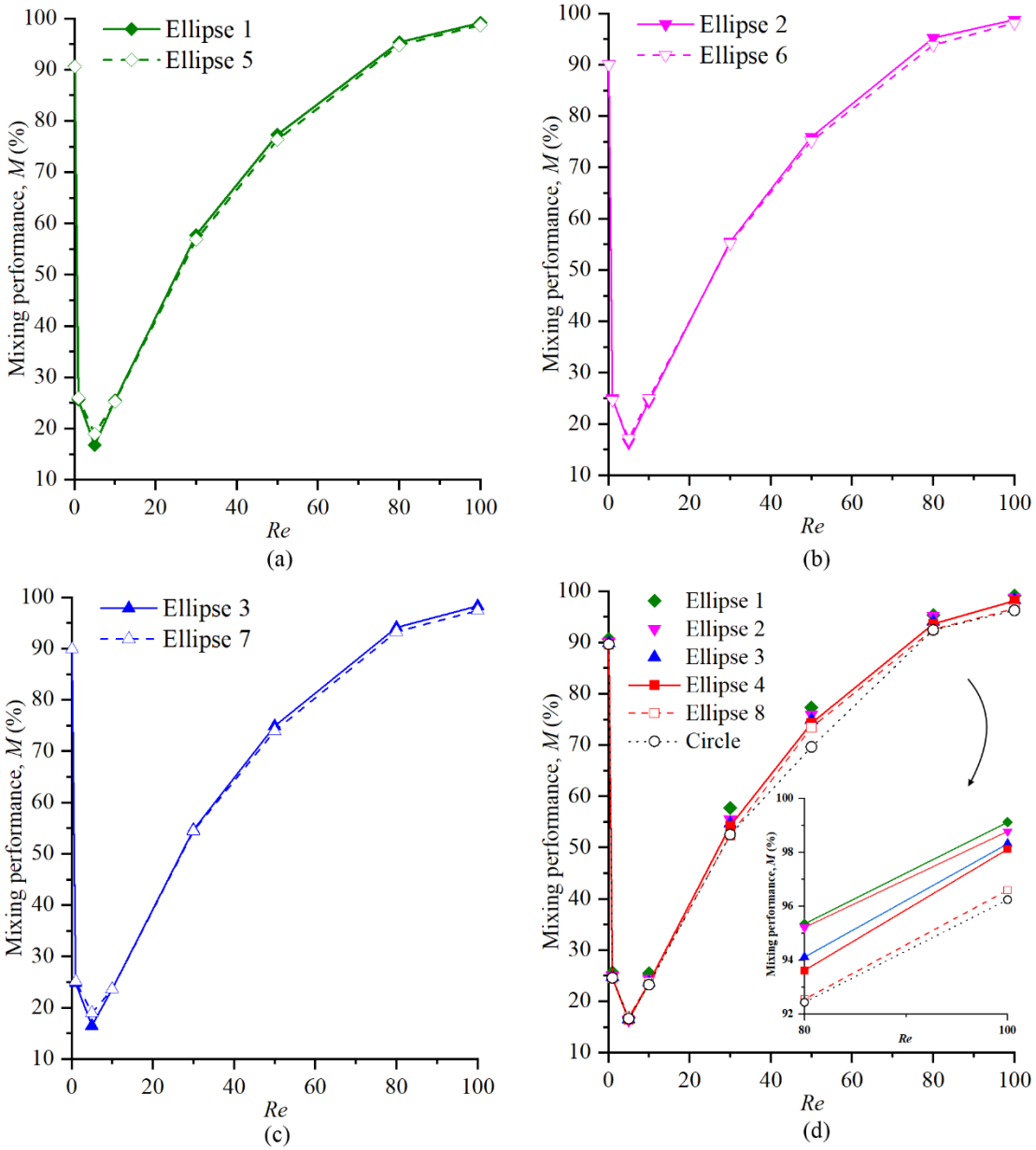

Fig. 8. Mixing performance of ellipse curve micromixers with *Re* from 0.1 to 100: (a) with ellipse 1 and 5, (b) with ellipse 2 and 6, (c) with ellipse 3 and 7, (d) with ellipse 4, ellipse 8 and the circle.

Fig. 8 exhibits the mixing performance of ellipse curve micromixers with *Re* from 0.1 to 100. As presented, all micromixers reach the highest mixing performance when *Re* = 100. Especially with ellipse 1 and 2, the ellipse curve micromixers can achieve a

mixing performance close to 99%. It is observed in Fig. 8(d) that the smaller the eccentricity, the lower the mixing performance. On conditions of a same eccentricity (results with the same color), better mixing performance are achieved in ellipses with foci on the X-axis than in ellipses with foci on the Y-axis. As presented in Fig. 8(d), the ellipse curve micromixer with ellipse 1 shows the highest mixing performance, while the micromixer with ellipse 8 has the lowest. By contrast, the mixing performance of circular serpentine micromixer is only about 95%, which is much lower than that of ellipse curve micromixers.

Constricted at micro scale, mixing only can be driven by molecular diffusion and chaotic advection. At a low Reynolds number, mixing is dominated by molecular diffusion. In this case, a lower flow velocity leads to a longer residence time, allowing molecular diffusion to fully develop, although it is essentially an inefficient process. As shown in Fig. 8, at $Re = 0.1$, the mixing performance of ellipse curve micromixers can reach more than 90%. Whereas the flow accelerates with *Re* increasing, the residence time is shortened and molecular diffusion is inevitably weakened. Mixing performance decreases and reaches the bottom at $Re = 5$. Afterwards, even if molecular diffusion continues to weaken with the increment of *Re*, mixing performance increases by the gradually enhanced chaotic advection.

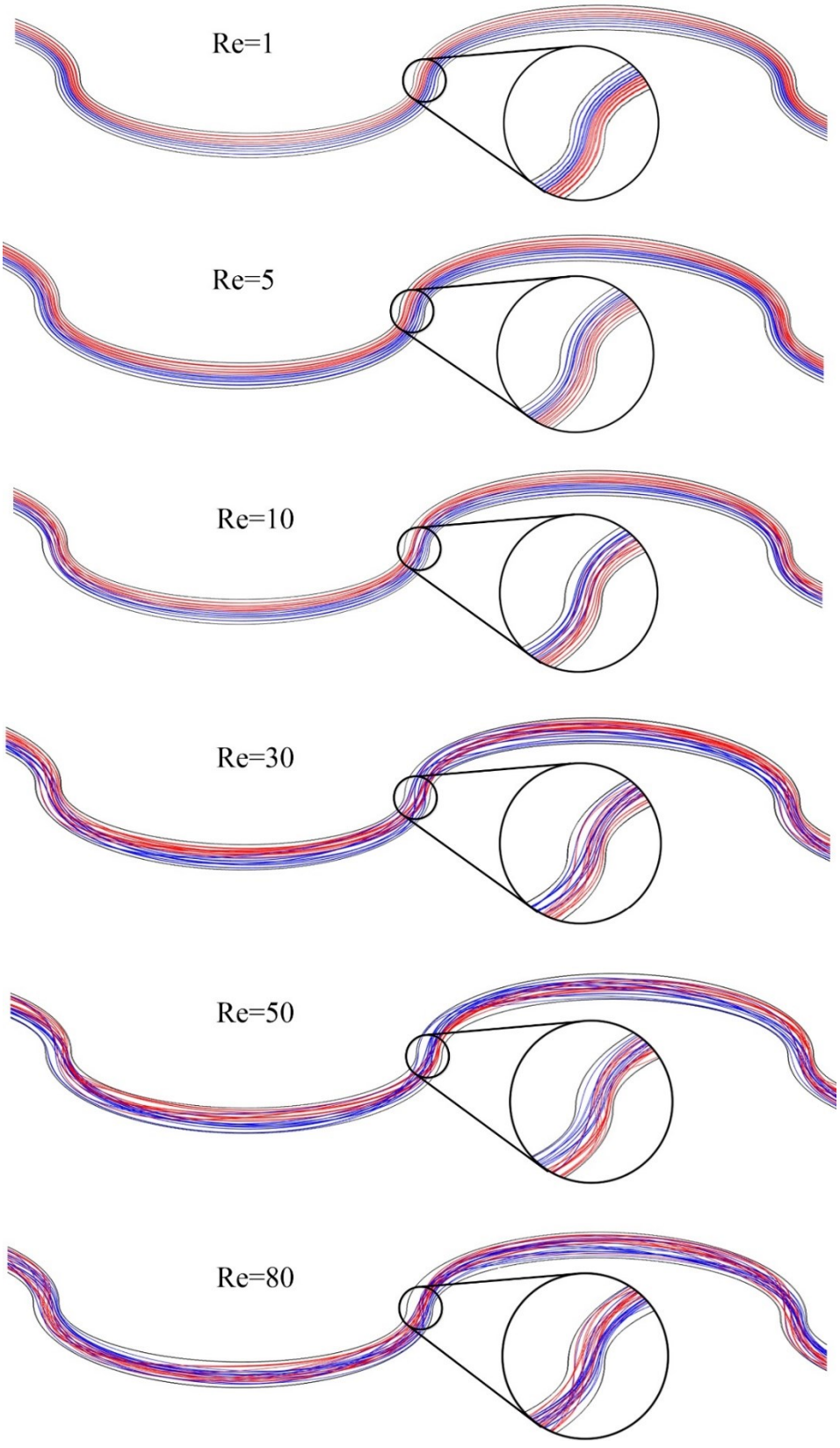

Fig. 9. Streamlines in the ellipse curve micromixer with *Re* from 1 to 80.

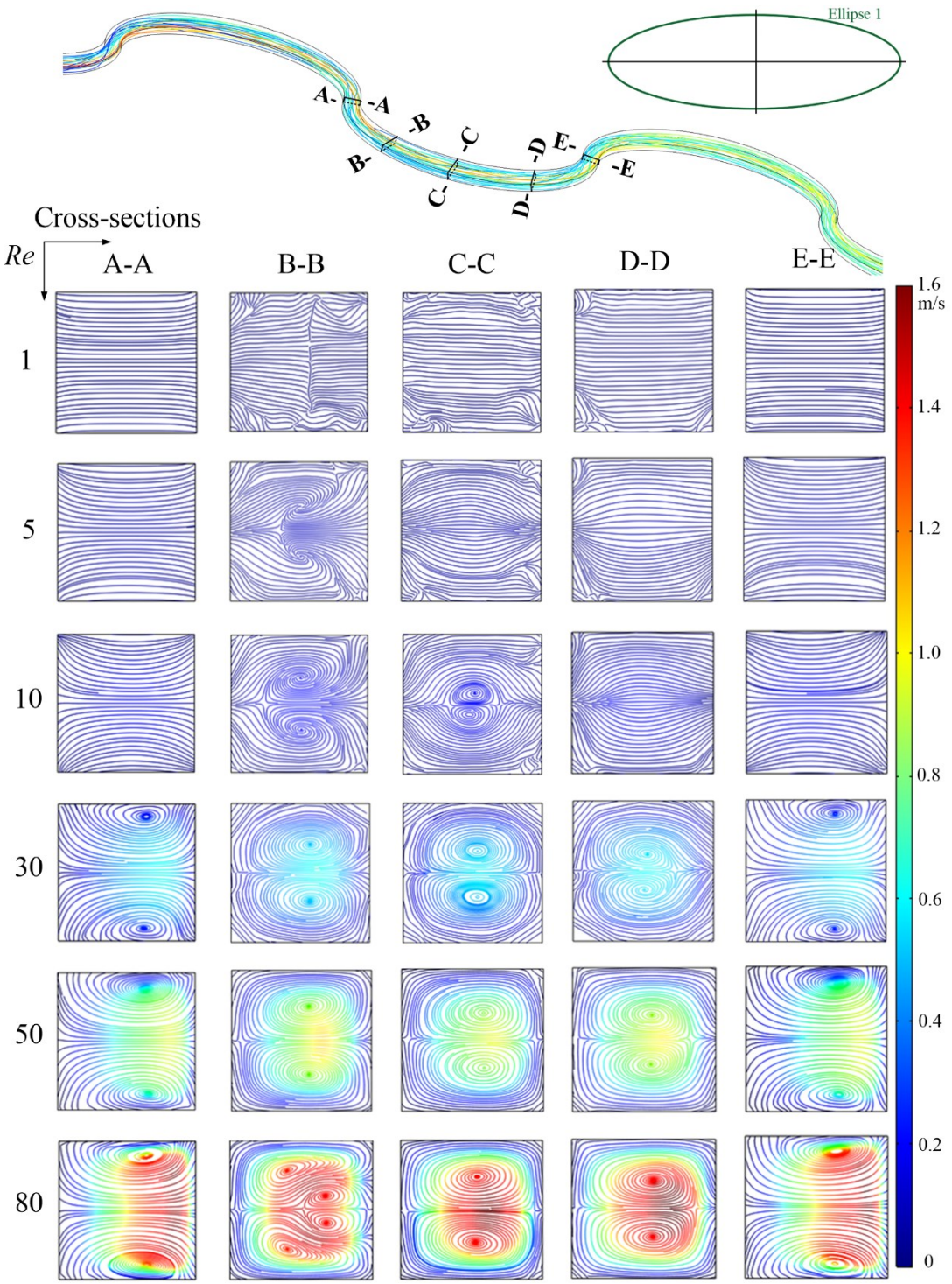

Fig. 10. Flow patterns of cross-sectional planes along the mixing unit with *Re* from 1 to 80.

Taking ellipse 1 as the example, Fig. 9 depicts the streamlines in the ellipse curve microchannel, and Fig. 10. draws the flow patterns of various cross-sections along one mixing unit. As presented in Fig. 9, although the streamlines start to get bended at *Re* =

5 and 10, the perturbation is slight and only can be noticed at the sharp turning positions. Streamlines are almost parallel where the ellipse curve is smooth. Likewise, as illustrated in Fig. 10, flow patterns are stable when *Re* is lower than 10, and only little vortices starts to generate at *Re* = 10. Chaotic advection is at the very beginning stage and makes little contribution to mixing.

When *Re* increases to 30, there are pronounced vortices that occupy the whole mixing unit (seen from Fig. 10). Meanwhile, violent distortion and intersection of streamlines clutter up the whole microchannels (seen from Fig. 9). The further increment of *Re* brings about more disordered streamlines and stronger vortices. It is observed from Fig. 10 that when *Re* = 80, two pairs of vortices are formed in cross-section B. The intense vortices strengthen the chaotic advection and plays a powerful boost to mixing. On the contrary to molecular diffusion, chaotic advection is a rapid and efficient process. As a result, mixing performance increases rapidly and almost reaches saturation at *Re* = 100.

6.1.2. Molecular diffusion and chaotic advection

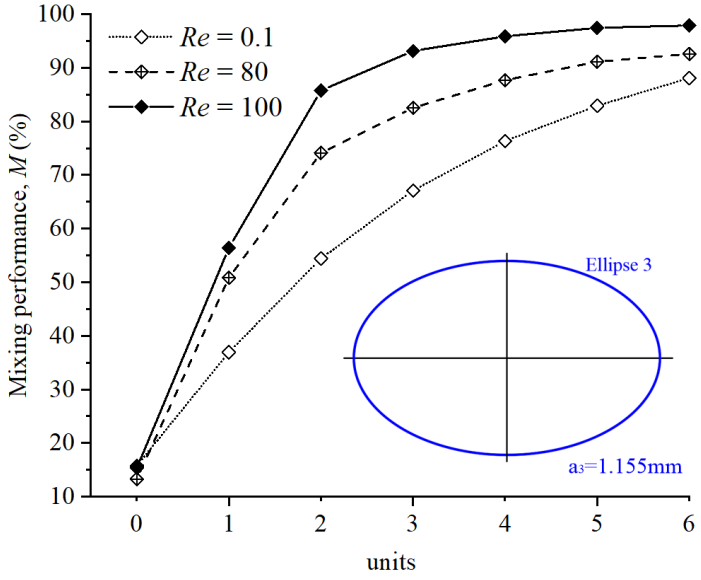

Fig. 11. Local mixing performance of the ellipse curve micromixer with ellipse 3 at *Re* = 0.1, 80 and 100.

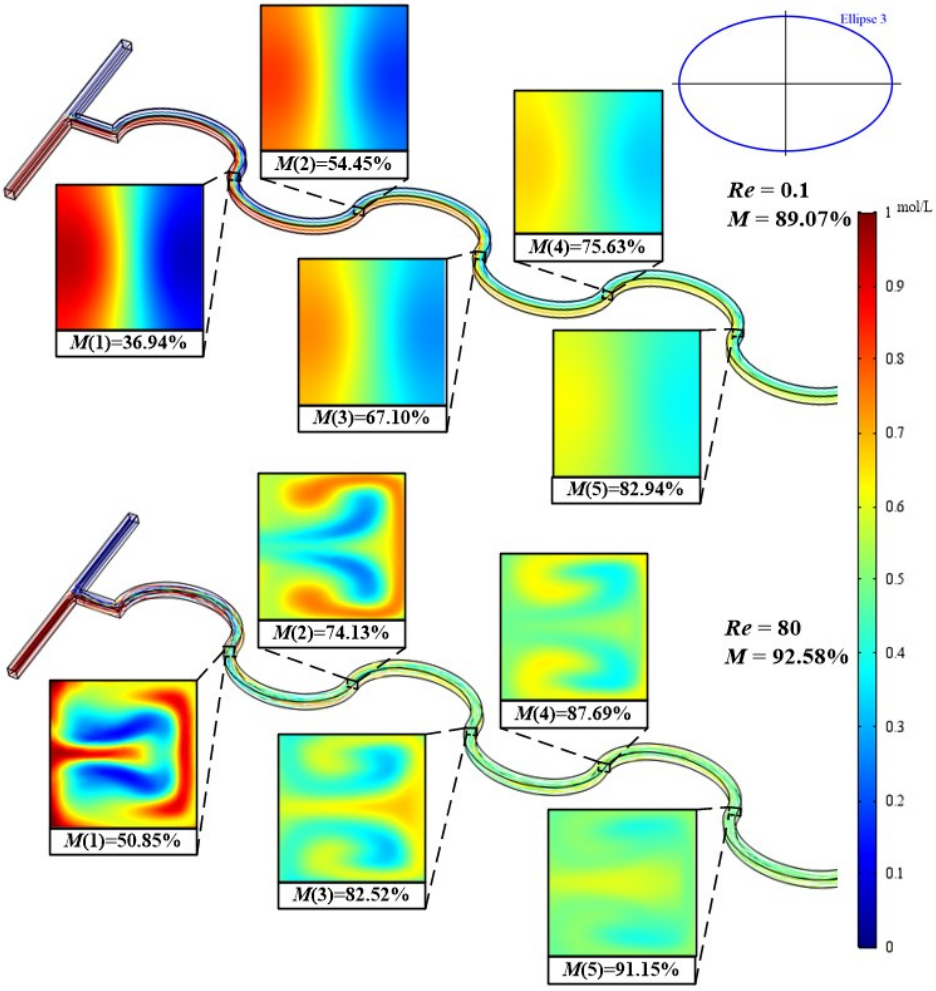

Fig. 12. Local mixing patterns of the ellipse curve micromixer with ellipse 3 at *Re* = 0.1 and 80.

As mentioned above, molecular diffusion and chaotic advection have different effects on mixing. Taking micromixer with ellipse 3 as an example, Fig. 11 shows the local mixing performance at *Re* = 0.1, 80 and 100, and local mixing patterns are compared in Fig. 12. As shown in Fig. 11, at *Re* = 80 and 100, mixing performance have a considerable increase in the former two mixing units. Owing to the intense chaotic advection, the contact area between the two reagents is expanded and the concentration difference has a sharp decline (seen from Fig. 12). Afterwards, the growth rate of mixing performance falls dramatically.

Moreover, it can be seen from Fig. 11 that when *Re* = 100, mixing performance has already exceeded 85 % after the former two mixing units. Hence, there is small room for the growth of mixing performance. Especially in the last mixing unit, the increment of mixing performance is less than 0.5 %. It is considered that mixing has already saturated, therefore no more mixing units are needed.

As presented in Fig. 12, when *Re* = 0.1, the contact area between the two reagents is restricted at the middle of microchannels. Molecular diffusion only slowly develops as the residence time increases. Since the molecular diffusion rate also depends on the concentration difference, the major increase of mixing performance is in the first mixing unit. Similarly, the increment of mixing decreases after each mixing unit, yet no dramatically falling like mixing at *Re* = 80 and 100. This is because the decrement of concentration difference is very slowly, when mixing is dominated by molecular diffusion.

Fig. 13 plots the residence time of mixing, which is the key influencing factor of molecular diffusion. Even if mixing performance at *Re* = 0.1 is close to 90 %, it takes more than 30 seconds to flow through the entire micromixer, which does not meet the requirement for rapid mixing. In contrast, mixing at *Re* =100 only needs 0.03 seconds.

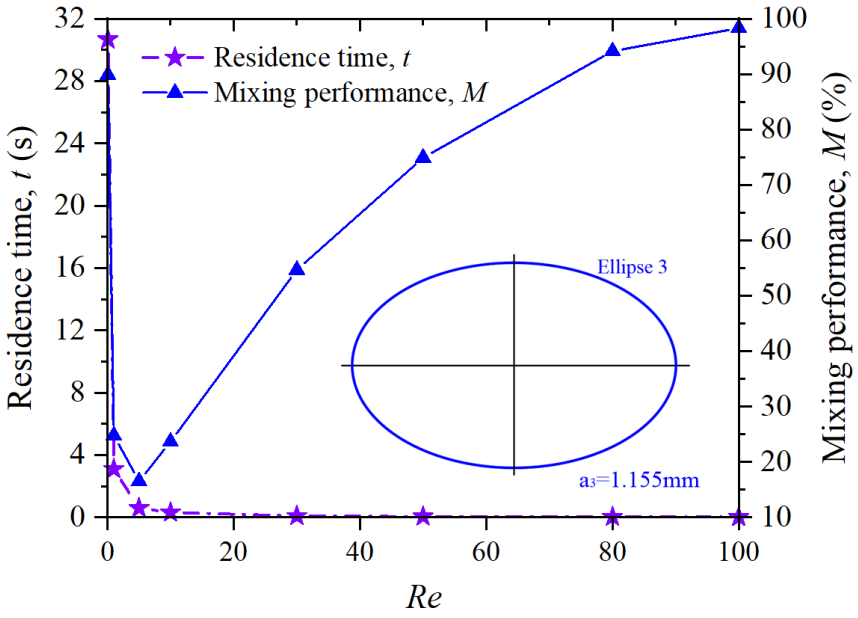

Fig. 13. Residence time of the ellipse curve micromixer with *Re* from 0.1 to 100.

6.2. Dean vortices and Dean numbers

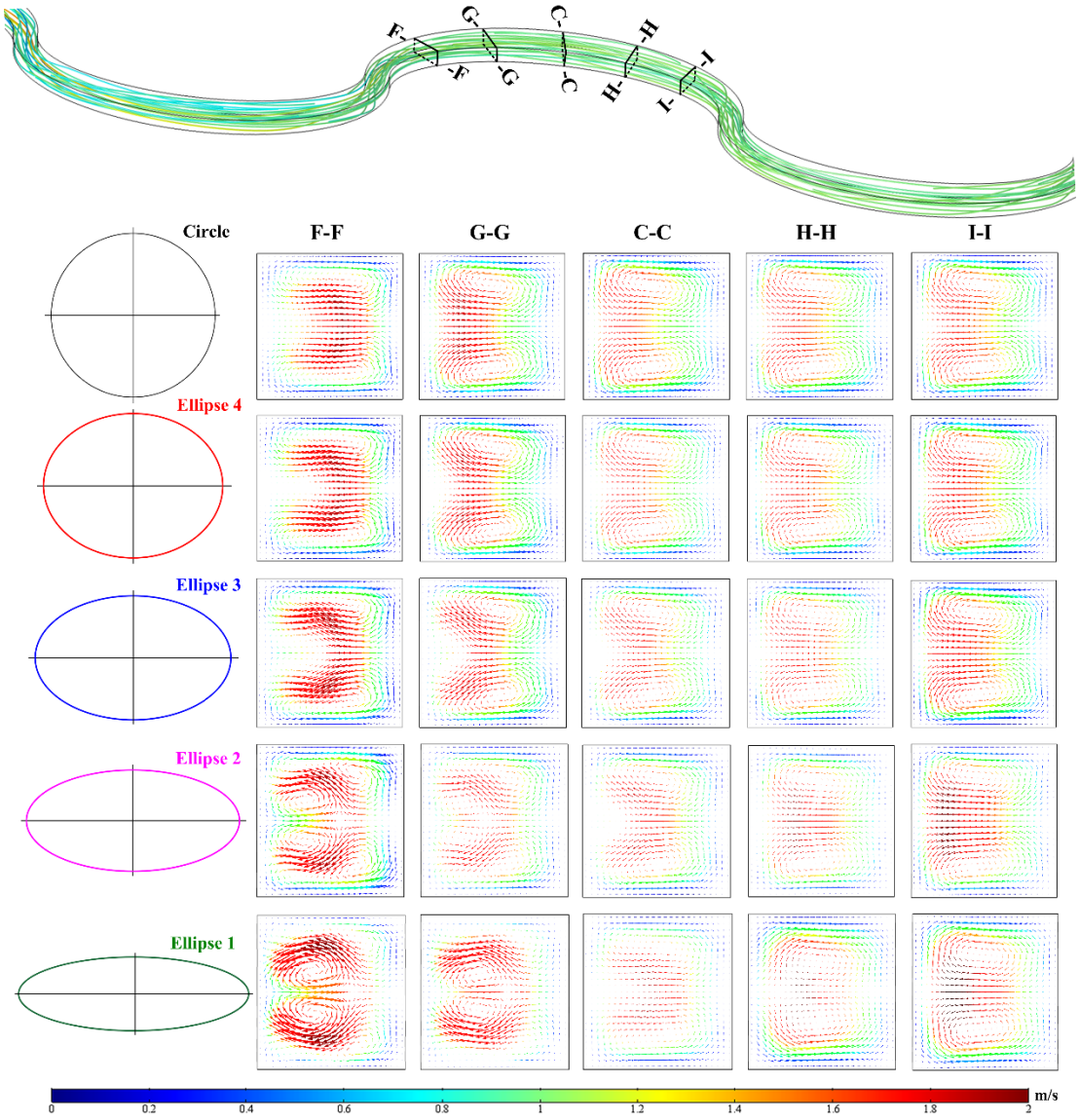

Fig. 14. Dean vortices formed along the ellipse curve microchannel at *Re* =100.

While fluids flowing through ellipse curve microchannels, the flow directions keep continuous changing. As shown in Fig. 14, under continuous effects of centrifugal force, Dean vortices are induced throughout the whole mixing unit. The flow patterns of Dean vortices vary with the ellipse curves, since the curvature of ellipse curve varies.

As presented in Fig.14, four visible vortices are formed at the F-F and G-G cross-sections in ellipses 1 and 2. Two vortices are at central region and the others are at

outside region. In ellipse 3, the two vortices at central region become indistinct and hard to be observed, although the two vortices at outside region are still clear. While in ellipse 4 and the circle, the two vortices at central region no longer exist. Only the two vortices at outside region are formed. This is because ellipses 1 and 2 have large curvature, the centrifugal force is strong and Dean vortices are strengthened.

Since the centrifugal force points to opposite directions in two continuous mixing units, the direction of centrifugal force has just suffered a change of 180 degrees when passing through the connection of two mixing units. Therefore, F-F and G-G cross-sections could generate two more Dean vortices at the central region, which are legacy of the previous mixing unit, but H-H and I-I cross-sections could not (seen from Fig. 14).

Furthermore, the intensity of Dean vortices can be quantitatively evaluated by Dean number (*De*), defined as Eq. (10).

$$D_e = \frac{\rho V D_h}{\mu}\left(\frac{\frac{D_h}{2}}{R}\right)^{1/2} \tag{10}$$

where, R represents the radius of curvature. Actually, R is the inverse of the curvature K, which can be calculated by Eq. (11) in the ellipse.

$$K = \frac{1}{R} = \frac{ab}{\left(a^2 \sin^2\theta + b^2 \cos^2\theta\right)^{3/2}} \tag{11}$$

where, θ is the angle between the X-axis and the line that connects the point on the ellipse curve and the center, as illustrated in Fig. 15.

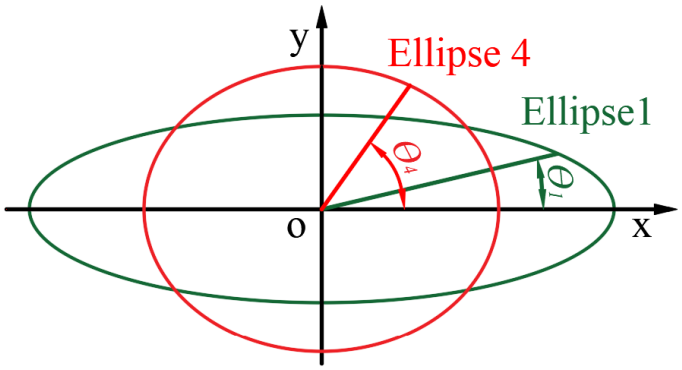

Fig. 15. Angle θ between the X-axis and the line that connects the point on the ellipse curve and the center.

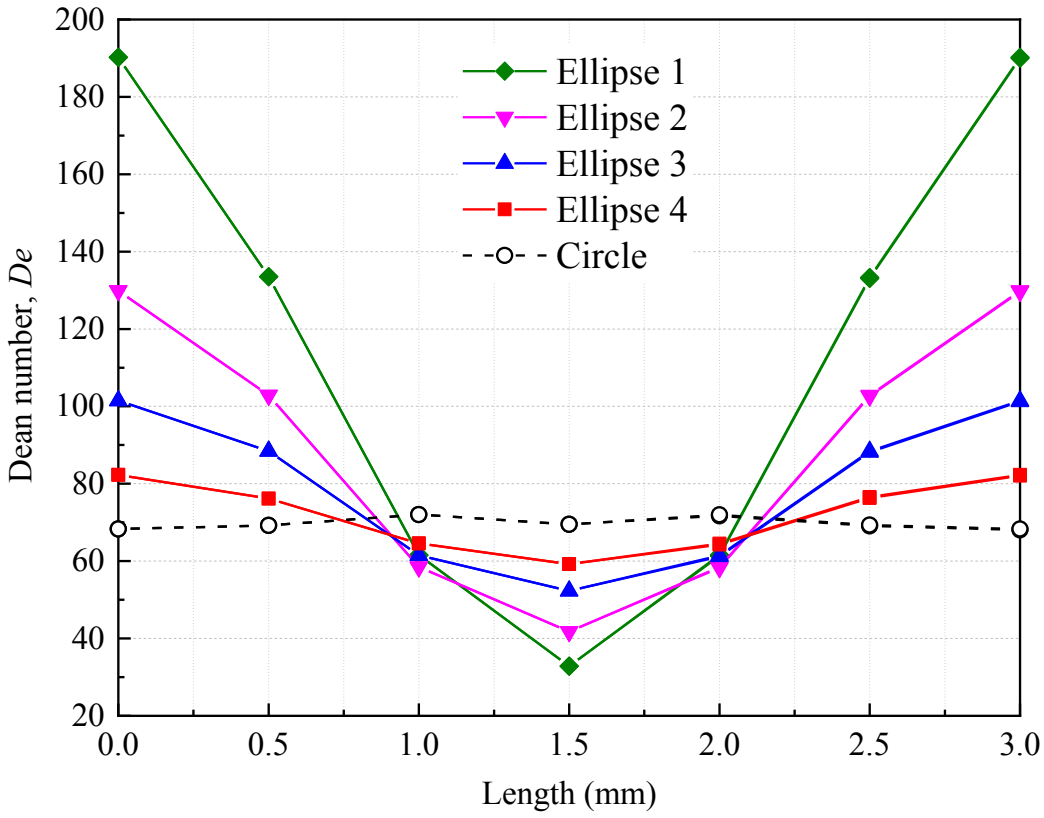

Fig. 16. Local Dean numbers in the third mixing unit at *Re* = 100.

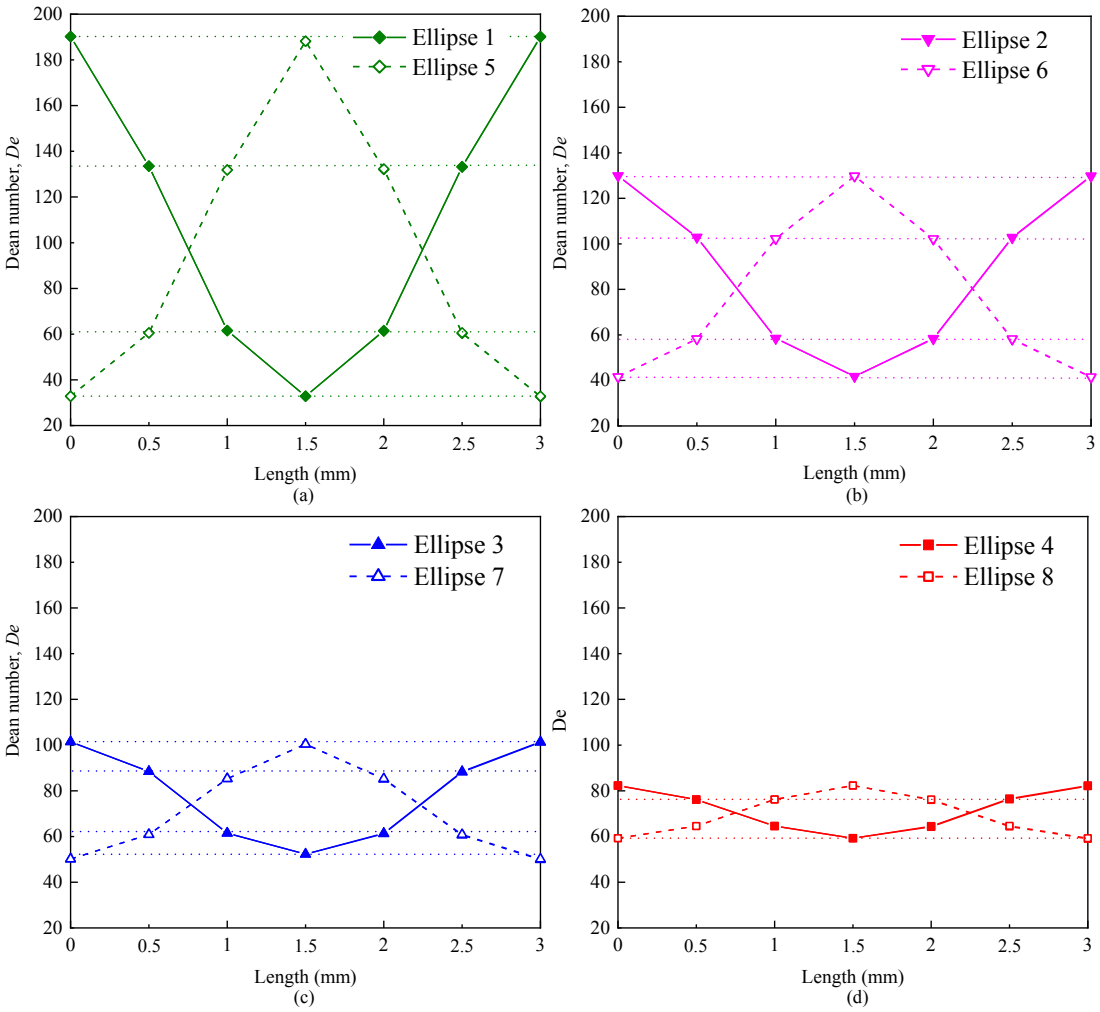

Fig. 17. Dean numbers of ellipses with foci on the X-axis and Y-axis: (a) with ellipse 1 and 5, (b) with ellipse 2 and 6, (c) with ellipse 3 and 7, (d) with ellipse 4 and ellipse 8.

While fluids flowing in the micromixer, the change in flow velocity (V) is less than 0.1 m s^{-1}, so Dean numbers are mainly affected by the radius of curvature (R). As shown in Fig. 16, both the largest and the smallest Dean number appear in the micromixer with ellipse 1. This is because ellipse 1 has the largest eccentricity, thus the radius of curvature (R) has a large range of variation. By contrast, in the micromixer with ellipse 4, Dean numbers have a small range of changes. While in the circular serpentine micromixer, Dean numbers are almost unchanged.

The enclosed area between Dean number and the X-axis reflects the total intensity of Dean vortices. Seen from Fig. 16, the strongest Dean vortices are induced in the micromixer with ellipse 1, which has the largest eccentricity. While in the micromixer with ellipse 4, Dean vortices is the weakest as a result of the smallest eccentricity. To a certain degree, the intensity of chaotic advection can be approximately evaluated by Dean numbers. Therefore, it is inferred that a larger eccentricity results in the more intense chaotic advection, and ultimately a better mixing performance.

As presented in Fig. 17, on conditions of a same eccentricity, Dean numbers of ellipses with foci on the X-axis (ellipse 1 to 4) are higher than that of ellipses with foci on the Y-axis (ellipse 5 to 8). This difference only comes from the flow velocity (V), because the curvature varies in the same range. The flow velocity is higher in ellipses with foci on the X-axis than in ellipses with foci on the Y-axis. Accordingly, ellipses with foci on the X-axis generate stronger Dean vortices, which also could interpret the difference of mixing performance between them.

6.3. Pressure drop

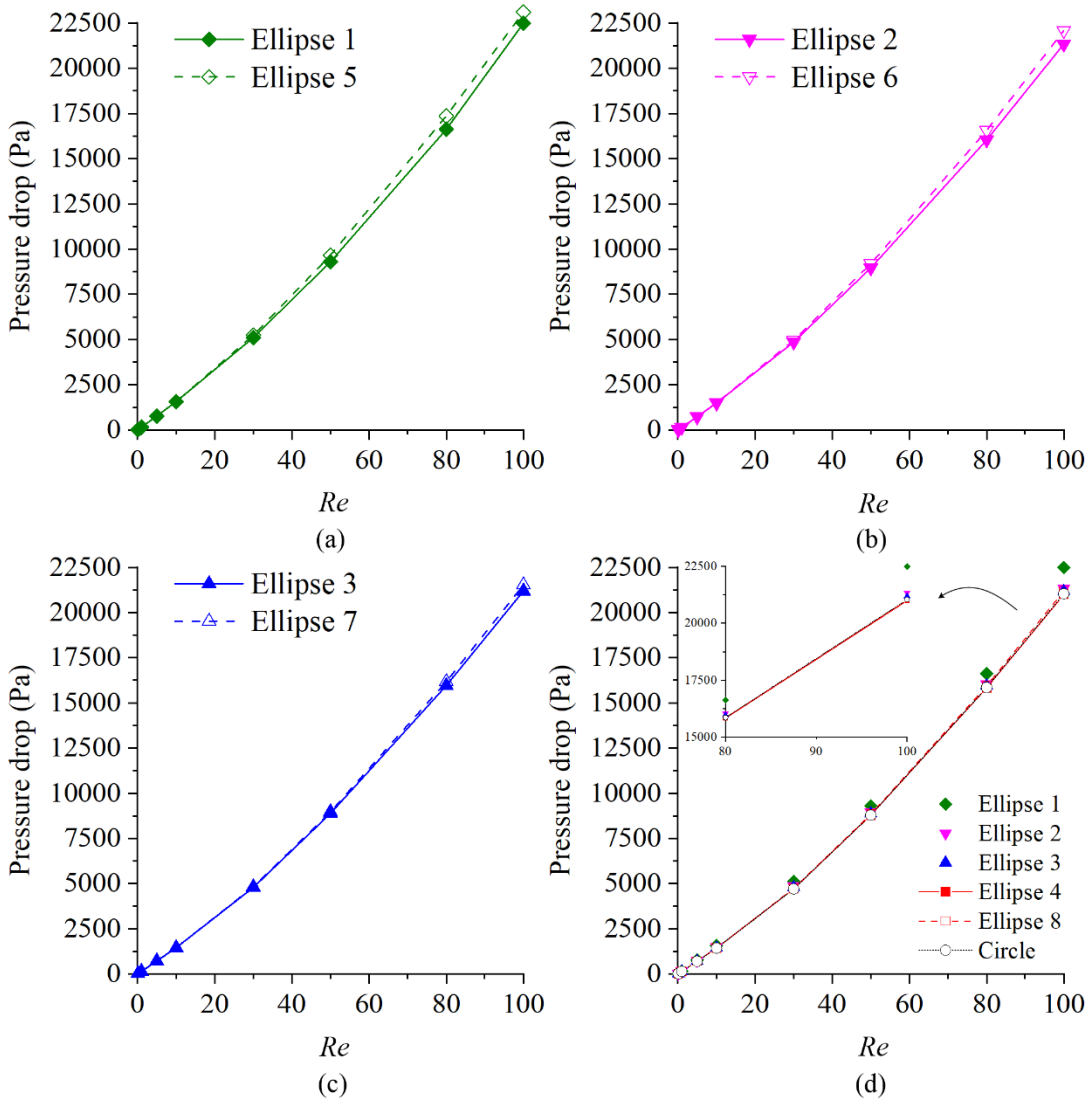

Fig. 18. Pressure drop of ellipse curve micromixers at *Re* from 0.1 to 100, (a) with ellipse 1 and 5, (b) with ellipse 2 and 6, (c) with ellipse 3 and 7, (d) with ellipse 4, ellipse 8 and the circle.

Considering the integration to a microfluidic system, it is an essential to control the pressure drop. Excessive pressure drop means more energy consumption, making the mixing with low cost-performance. On account of the intense vortices, more pressure drop is produced when mixing is dominated by chaotic advection. As presented in Fig. 18, pressure drop performs a rapid increase with *Re* increasing, because chaotic advection develops rapidly with the increment of *Re*.

As shown in Fig. 18(d), micromixer with ellipse 1 that has the largest eccentricity yields the highest pressure drop. The larger changes in curvature not only produce stronger chaotic advection, but also consume more energy. On the other hand, ellipses with foci on the X-axis (ellipse 1 to 4) yields less pressure drop than those with foci on the Y-axis (ellipse 5 to 8), on conditions of a same eccentricity (results with the same color).

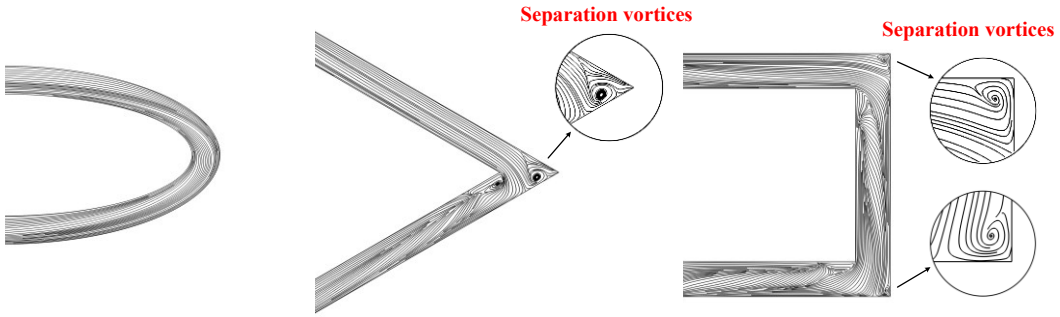

(a) Ellipse curve micromixer with ellipse 5 (b) Zigzag micromixer (c) Square-wave micromixer

Fig. 19. Streamlines of the (a) ellipse curve micromixer with ellipse 5, (b) zigzag micromixer and (c) square-wave micromixer at $Re = 100$.

For comparison, zigzag and square-wave serpentine micromixers has also been investigated. Taking the ellipse curve micromixer with ellipse 5 as an example, which has the largest eccentricity. As plotted in Fig. 19, visible separation vortices are formed at the sharp turns in zigzag and square-wave microchannels. While in the ellipse curve micromixer, there are no separation vortices even at a turn with the largest curvature.

The separation vortices promote the chaotic advection, but tend to induce significant pressure drop. As shown in Fig. 20(b), the pressure drop of zigzag serpentine micromixer is more than 2.5×10^4 Pa at $Re = 100$. While in the square-wave serpentine micromixer, the pressure drop even exceeds 2.9×10^4 Pa. In contrast, the highest

pressure drop of the ellipse curve micromixer is still below 2.3×10^4 Pa. This means that the energy consumption is much lower than that of the zigzag and square-wave serpentine micromixers.

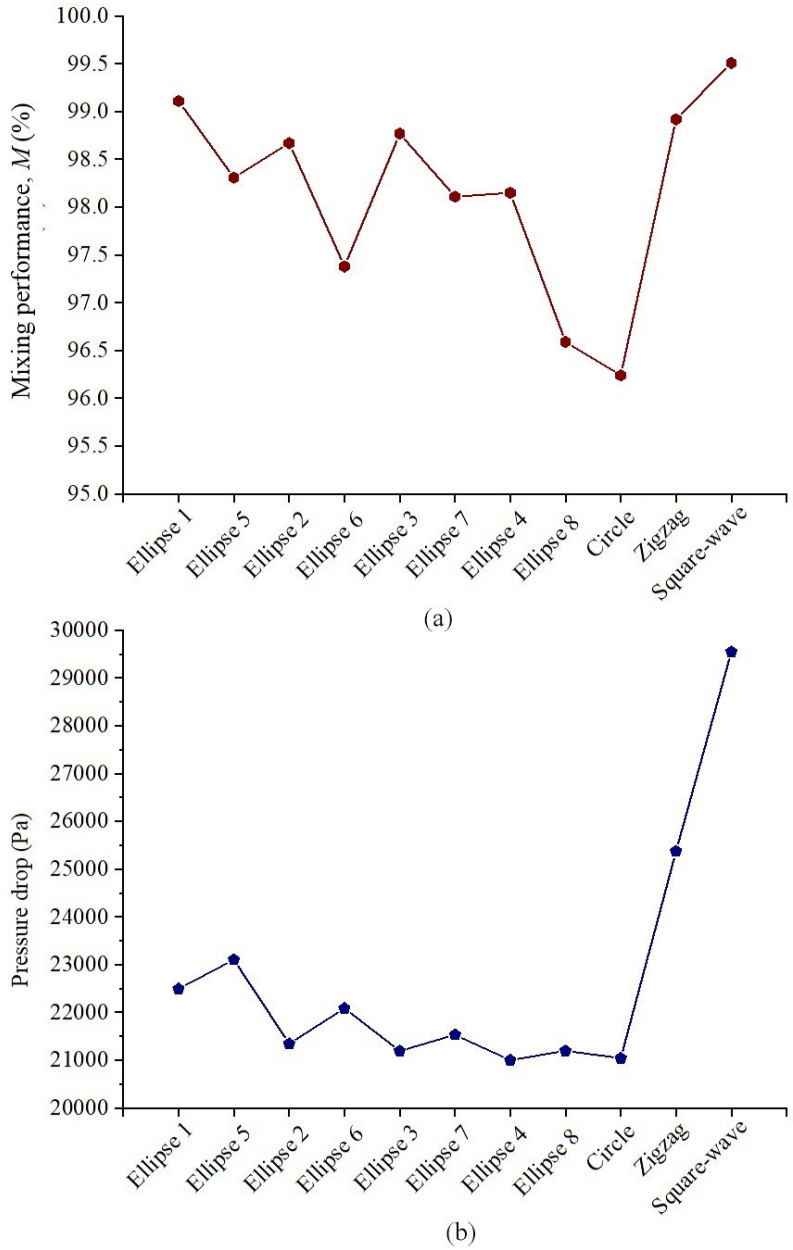

Fig. 20. (a) Mixing performance and (b) pressure drop of the ellipse curve, circular, zigzag and square-wave micromixers at $Re = 100$.

As exhibited in Fig. 20(a), when $Re = 100$, zigzag serpentine micromixer can

achieve mixing performance close to 99 %, while in the square-wave one is near 100 %. In comparison, ellipse curve micromixers with ellipse 1 to 5 could achieve similar mixing performance to the zigzag micromixer, although there are no separation vortices formed. Especially in the micromixer with ellipse 1, mixing performance exceeds 99 % at Re = 100, which is higher than that of the zigzag micromixer.

Fig. 21 exhibits the local mixing performance and local pressure drop of ellipse curve, circular, zigzag and square-wave micromixers at Re = 100. Taking the mixing performance of 98% as a standard, the square-wave micromixer could reach it after four mixing units, as seen from Fig. 21(a). While for the ellipse curve micromixer with ellipse 1, ellipse 2, and the zigzag micromixer, five mixing units are needed to achieve this standard. As shown in Fig. 21(b), even if ellipse 1 and ellipse 2 needs five mixing units to achieve the mixing performance of 98%, the pressure drop they generated are still much lower than that of the square-wave micromixer after four mixing unit, and lower than that of the zigzag micromixer.

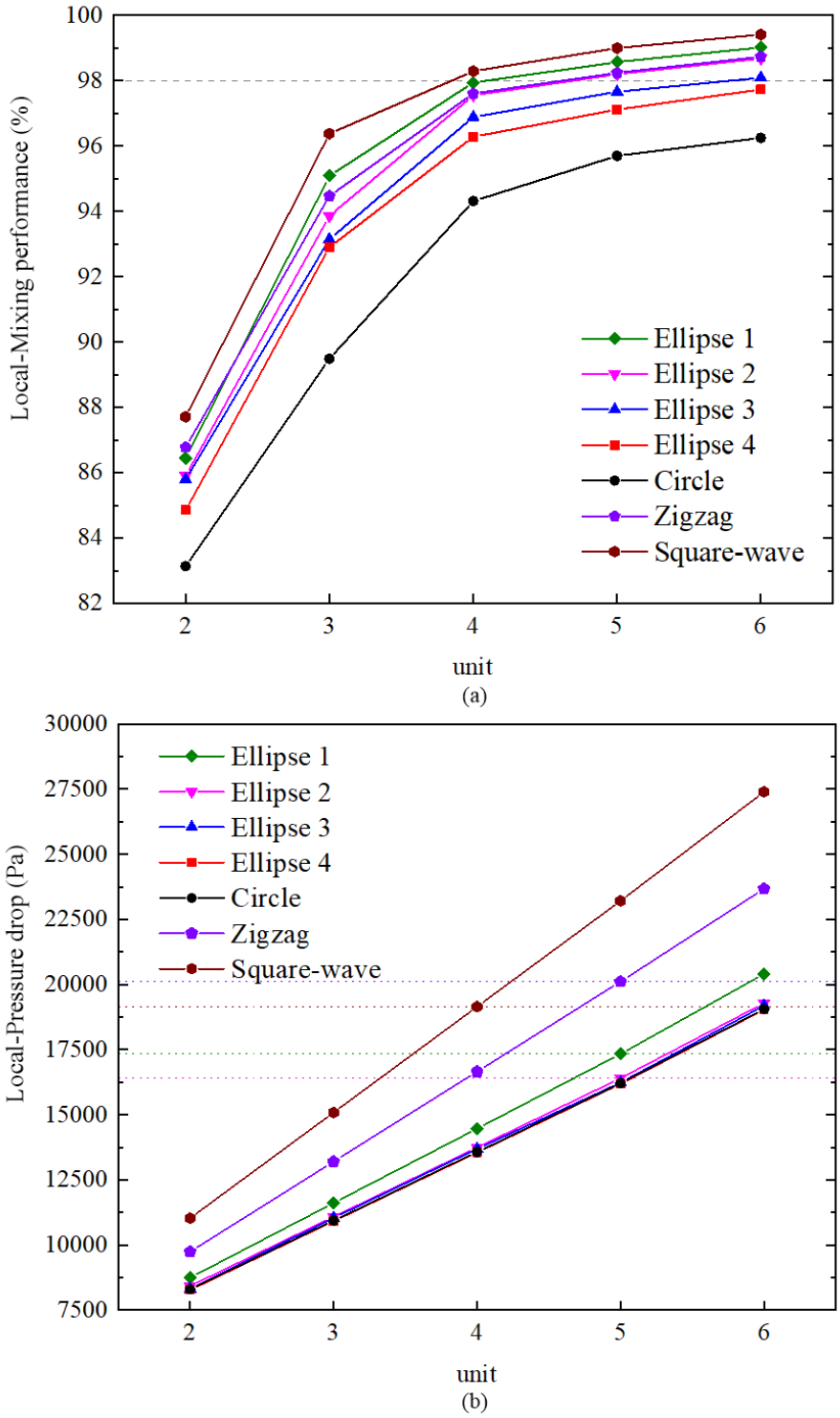

Fig. 21. (a) Local Mixing performance and (b) local pressure drop of ellipse curve, circular, zigzag and square-wave micromixers at *Re* = 100.

6.4. Mixing efficiency cost

For an intuitive evaluation of cost-performance, a novel parameter named mixing efficiency cost (*Mec*) is put forward, defined by Eq. (12).

$$Mec = 1/\frac{100M}{PD \cdot t} = \frac{PD \cdot t}{100M} \tag{12}$$

where, M is the mixing performance, PD the pressure drop and t denotes the residence time. According to Eq. (12), mixing efficiency cost (*Mec*) means the time and pressure drop required per unit of mixing performance. In a word, a lower *Mec* implies the higher cost-performance and a more cost-effective micromixer.

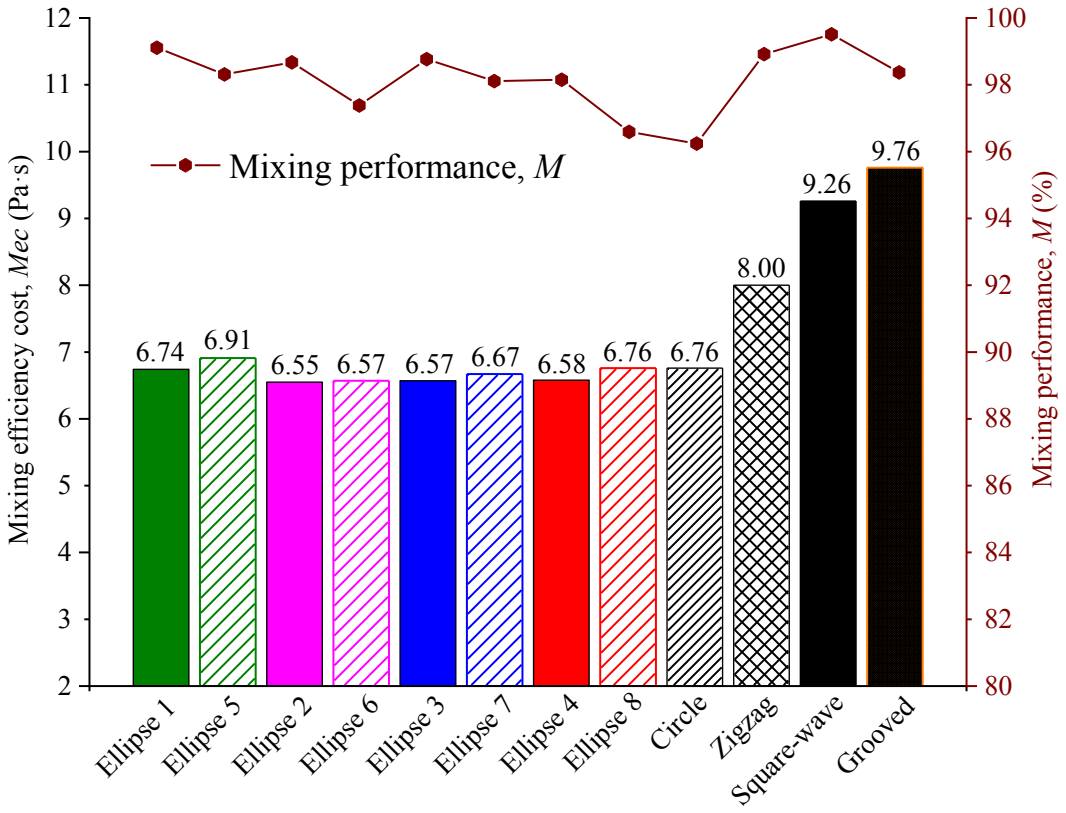

Fig. 22. Mixing efficiency cost (*Mec*) of ellipse curve, circular, zigzag, square-wave and grooved [30] micromixers at $Re = 100$.

As exhibited in Fig. 22, on conditions of a same eccentricity, ellipses with foci on the X-axis (ellipses 1 to 4) show lower mixing efficiency cost (*Mec*) than those with foci on the Y-axis (ellipses 5 to 8). The underlying reason is that the ellipse with foci

on the X-axis can achieve higher mixing performance and simultaneously produce lower pressure drop. Owing to the strongest chaotic convection, the ellipse micromixer with the largest eccentricity (ellipse 1 and 5) has the highest mixing efficiency cost (*Mec*), but it is still far lower than that of the zigzag and square-wave micromixer.

When compared with the grooved serpentine micromixer proposed by K. J. Cook [30], the ellipse curve micromixer still indicates significant advantages on the cost-performance. The mixing efficiency cost (*Mec*) of the grooved serpentine micromixer is even higher than that of the square-wave one. Additionally, it can be inferred from Fig. 22 that the ellipse curve micromixer with ellipse 2 is the most cost-effective one. The moderate eccentricity of ellipse 2 leads to affordable pressure drop while still maintain an excellent mixing performance.

7. Conclusions

The paper proposed a cost-effective serpentine micromixer utilizing ellipse curve. In ellipse curve microchannels, the flow directions keep changing, therefore Dean vortices are induced throughout the flow path. Numerical simulation and visualization experiments were conducted to investigate the mixing process of micromixers with various ellipse shapes. It is found that most ellipse curve micromixers can achieve a mixing performance close to 99% at $Re = 100$. When $Re \geq 80$ or $Re \leq 0.1$, a mixing performance about 90% can be reached, but the mixing dominated by molecular diffusion at a low *Re* is time-consuming and inefficient. Among the various ellipse shapes, ellipse with a larger eccentricity induce stronger Dean vortices, thus a better

mixing performance is obtained. Meanwhile, on conditions of a same eccentricity, ellipses with foci on the X-axis can achieve better mixing performance and lower pressure drop than those on the Y-axis.

Besides, it is concluded that the continuous and smooth changing curvature of ellipse curves mitigates excessive pressure drop in zigzag and square-wave microchannels. The ellipse curve micromixer can produce lower pressure drop while simultaneously maintain excellent mixing performance. To evaluate the cost-performance of micromixers, a parameter named mixing efficiency cost (*Mec*) is proposed. Compared with the zigzag, square-wave and grooved serpentine micromixer, the ellipse curve micromixer demonstrates much lower mixing efficiency cost (*Mec*). It means that the ellipse curve micromixer is a more cost-effective choice for rapid mixing in microfluidic systems.

Acknowledgements

The authors would like to acknowledge the financial support from the National Natural Science Foundation of China (No. 91860207). This work was also supported by grants from Taishan Scholar Foundation and Shandong Provincial Natural Science Foundation (ZR2019MEE073 and 2019JMRH0307).

References

[1] Y. Liu, X. Jiang, Why microfluidics? Merits and trends in chemical synthesis, Lab Chip 17 (23) (2017) 3960-3978.

[2] E. Mielke, D.M. Roberge, A. Macchi, Microreactor mixing-unit design for fast

liquid–liquid reactions, J. Flow Chem. 6 (2016) 279-287.

[3] C.Y. Lee, L.M. Fu, Recent advances and applications of micromixers, Sens. Actuators B: Chem. 259 (2018) 677-702.

[4] M.X. Lin, K.A. Hyun, H. Moon, T. Sim, J. Lee, J. Park, S. Lee, H. Jung, Continuous labeling of circulating tumor cells with microbeads using a vortex micromixer for highly selective isolation, Biosens. Bioelectron. 40 (2013) 63-67.

[5] C.H. Lin, Y.N. Wang, L.M. Fu, Integrated microfluidic chip for rapid DNA digestion and time-resolved capillary electrophoresis analysis, Biomicrofluidics 6 (2012) 012818.

[6] W.B. Lee, Y.H. Chen, H.I. Lin, S.C. Shiesh, G.B. Lee, An integrated microfluidic system for fast, automatic detection of C-reactive, Protein Sens. Actuators B: Chem. 157 (2011) 710-721.

[7] J. Nam, C.S. Lim, Micromixing using swirling induced by three-dimensional dual surface acoustic waves (3D-dSAW), Sens. Actuators B: Chem. 255 (2018) 3434-3440.

[8] M. Nazari, S. Rashidi, J. Abolfazli, Mixing process and mass transfer in a novel design of induced-charge electrokinetic micromixer with a conductive mixing chamber, Int. Commun. Heat Mass Transf. 108 (2019) 104293.

[9] G. Kunti, A. Bhattacharya, S. Chakraborty, Rapid mixing with high-throughput in a semi-active semi-passive micromixer, Electrophoresis 38 (2017) 1310-1317.

[10] M. Zhang, W. Zhang, Z. Wu, Y. Shen, Y. Chen, C. Lan, F. Li, W. Cai, Comparison of micro-mixing in time pulsed newtonian fluid and viscoelastic fluid, Micromachines 10 (4) (2019) 262.

[11] C. Kumar, M. Hejazian, C. From, S.C. Saha, E. Sauret, Y. Gu, N.-T. Nguyen,

Modeling of mass transfer enhancement in a magnetofluidic micromixer, Phys. Fluids 31 (6) (2019) 063603.

[12] X. Chen, Z. Zhao, Numerical investigation on layout optimization of obstacles in a three-dimensional passive micromixer, Anal. Chim. Acta 964 (2017) 142-149.

[13] S. Zhang, X. Chen, Z. Wu, Y. Zheng, Numerical study on stagger Koch fractal baffles micromixer, Int. J. Heat Mass Transf. 133 (2019) 1065-1073.

[14] M. Jain, A. Rao, K. Nandakumar, Numerical study on shape optimization of groove micromixers, Microfluid. Nanofluid. 15 (5) (2013) 689-699.

[15] S. Hossain, I. Lee, S.M. Kim, K.Y. Kim, A micromixer with two-layer serpentine crossing channels having excellent mixing performance at low Reynolds numbers, Chem. Eng. J. 327 (2017) 268-277.

[16] L.M. Fu, W.C. Fang, H.H. Hou, Y.N. Wang, T.F. Hong, Rapid vortex microfluidic mixer utilizing double-heart chamber, Chem. Eng. J. 249 (2014) 246-251.

[17] A. Alam, K.Y. Kim, Mixing performance of a planar micromixer with circular chambers and crossing constriction channels, Sens. Actuators B: Chem. 176 (1) (2013) 639-652.

[18] G.D. Xia, J. Li, X.P. Tian, M.Z. Zhou, Analysis of flow and mixing characteristics of planar asymmetric split-and-recombine (P-SAR) micromixers with fan-shaped cavities, Ind. Eng. Chem. Res. 51 (2012) 7816-7827.

[19] X. Wang, Z. Liu, B. Wang, Q. Song, Investigations into planar splitting and recombining micromixers with asymmetric structures, J. Micromech. Microeng. 30 (1) (2020) 015006.

[20] I. Shah, S.W. Kim, K. Kim, Y.H. Doh, K.H. Choi, Experimental and numerical analysis of Y-shaped split and recombination micro-mixer with different mixing units, Chem. Eng. J. 358 (2019) 691-706.

[21] S. Hossain, M.A. Ansari, K.Y. Kim, Evaluation of the mixing performance of three passive micromixers, Chem. Eng. J. 150 (2) (2009) 492-501.

[22] S. Elmas, A. Pospisilova, A.A. Sekulska, V. Vasilev, T. Nann, S. Thornton, C. Priest, Photometric Sensing of Active Chlorine, Total Chlorine, and pH on a Microfluidic Chip for Online Swimming Pool Monitoring, Sensors 20 (11) (2020) 3099.

[23] V. Mengeaud, J. Josserand, H.H. Girault, Mixing processes in a zigzag microchannel: finite element simulations and optical study, Anal. Chem. 74 (16) (2002) 4279-4286.

[24] X. Chen, T. Li, A novel passive micromixer designed by applying an optimization algorithm to the zigzag microchannel, Chem. Eng. J. 313 (2017) 1406-1414.

[25] X. Chen, T. Li, A novel design for passive micromixers based on topology optimization method, Biomed. Microdevices 18 (4) (2016) 1-15.

[26] S. Hossain, K.Y. Kim. Mixing performance of a serpentine micromixer with non-aligned inputs, Micromachines 6 (7) (2015) 842-854.

[27] J.N. Kuo, L.R. Jiang, Design optimization of micromixer with square-wave microchannel on compact disk microfluidic platform, Microsyst. Technol. 20 (2014) 91-99.

[28] A. Shamloo, M. Madadelahi, A. Akbari, Numerical simulation of centrifugal serpentine micromixers and analyzing mixing quality parameters, Chem. Eng. Process.

104 (2016) 243-252.

[29] J.A. Clark, T.A. Butt, G. Mahajan, C.R. Kothapalli, M. Kaufman, P.S. Fodor, Performance and implementation of centrifugal serpentine micromixers with non-rectangular cross-section, J. Micromech. Microeng. 29 (7) (2019) 075012.

[30] K. J. Cook, Y. Fan, I. Hassan, Mixing evaluation of a passive scaled-up serpentine micromixer with slanted grooves, J. Fluids Eng. 135 (8) (2013) 081102.

[31] T. Rhoades, C. R. Kothapalli, P. S. Fodor, Mixing Optimization in Grooved Serpentine Microchannels, Micromachines 11 (1) (2020) 61.

[32] X. Chen, T. Li, H. Zeng, Z. Hu, B. Fu, Numerical and experimental investigation on micromixers with serpentine microchannels, Int. J. Heat Mass Transf. 98 (2016) 131-140.

[33] M. K. Parsa, F. Hormozi, Experimental and CFD modeling of fluid mixing in sinusoidal microchannels with different phase shift between side walls, J. Micromech. Microeng. 24 (6) (2014) 065018.

[34] M. U. Javaid, T. A. Cheema, C. W. Park, Analysis of passive mixing in a serpentine microchannel with sinusoidal side walls, Micromachines 9 (1) (2018) 8.